

# Compact Series Visco-Elastic Joint (SVEJ) for Smooth Torque Control

Domenico Chiaradia<sup>✉</sup>, Luca Tiseni<sup>✉</sup>, and Antonio Frisoli<sup>✉</sup>

**Abstract**—The design and control of a new series-viscous-elastic joint are presented. The proposed joint consists of 3D printed parts compressing nonlinear elastic silicone springs. The use of silicone springs is the main novelty of the system; they exhibit internal damping, which enhances system performance allowing a simpler and more stable control. Their stiffness allows the system to bear a torque of about 4.5 Nm at a deformation angle of about 20 degrees. In this article, the system is modeled using the Neo-Hookean material model and then characterized through experiments to build the joint torque estimator. A proportional torque controller is implemented to evaluate bandwidth, transparency, impedance rendering, and stability, obtaining satisfactory results. The bandwidth ranges from 6.9 to 9.9 Hz depending on chirp input torque amplitude, as the system is nonlinear. The proposed solution is compact and cheap; both the design and the torque controller are suitable for future integration in an exoskeleton, or a cooperative robot, or a haptic device. SVEJ works as a torque sensor and introduces compliance between the motor and the environment, enhancing safety for robotic devices interacting with humans.

**Index Terms**—Series visco-elastic joint, torque sensor, physical human-robot interaction, torque control.

## I. INTRODUCTION

IN physical human-robot interaction (pHRI), the use of compliant actuators is widely studied and adopted, especially for applications like rehabilitation [1], assistance [2], human-friendly robot designs [3] and haptic devices [4]. Compliance in robotic joints provides many benefits, such as shock tolerance, more accurate force control, and passive energy storage. Moreover, it is useful to preserve safety in human-robot interaction [5], and to relax the requirements of the main actuator [6].

It is possible to achieve joint compliance interposing a Series Elastic element between the Actuator and the link (SEA) [7], or, in general, adding a physical impedance. Both stiffness and impedance can be fixed or variable, as in the case of the Variable Stiffness Actuators (VSAs) [8] or the more general Variable Impedance Actuators (VIAs) [9]. The variable

Manuscript received September 27, 2019; revised January 3, 2020; accepted January 20, 2020. Date of publication January 30, 2020; date of current version March 17, 2020. This article was recommended for publication by Associate Editor Dr. C. Basdogan and Editor-in-Chief Dr. L. Jones upon evaluation of the reviewers' comments. (Domenico Chiaradia and Luca Tiseni contributed equally to this work.) (Corresponding author: Domenico Chiaradia.)

The authors are with the PERCRO Laboratory, TeCIP Institute, Sant'Anna School of Advanced Studies, 56127 Pisa, Italy (e-mail: domenico.chiaradia@santannapisa.it; luca.tiseni@santannapisa.it; a.frisoli@sssup.it).

This article has supplementary downloadable material available at <https://ieeexplore.ieee.org>, provided by the authors.

Digital Object Identifier 10.1109/TOH.2020.2970912

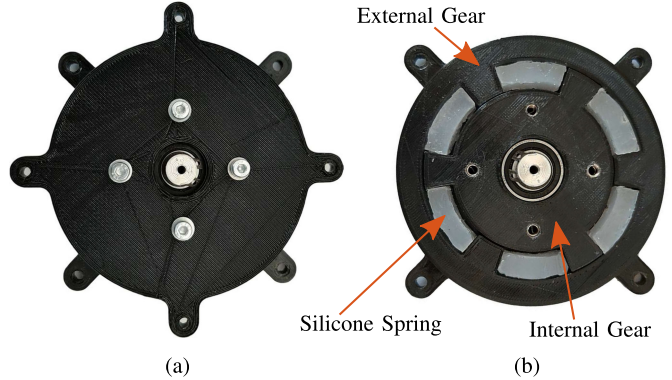


Fig. 1. Pictures of the SVEJ: a) whole covered system; b) uncovered system with the arrangement of external gear, internal gear, and silicone springs.

stiffness/impedance actuators have the main advantage of allowing the setting of both the interaction behavior and the torque measurement resolution. However, this “flexibility” comes at the cost of a bulky and more complex design, because it requires an additional actuator or adjustment mechanisms, or both. On the opposite, SEA uses linear springs, usually metallic ones, that exhibit a fixed mapping between deflection measurement and joint torque. Thus, SEAs can be very compact, robust, and cheap, but their design is the trade-off of fixed torque measurement resolution [10], achievable rendering impedance, impact absorption, and actuation bandwidth [11].

Nonlinear SEAs can overcome some of the linear SEA limitations [12]. For example, Malzahn [13] designed a rolling flexure mechanism to increase the stiffness of the joint progressively; in this way, it is possible to obtain high torque measurement resolution at both low and high joint stiffnesses. High resolution for a wide range of stiffness is convenient for enhancing torque control, which is one of the main reasons for introducing compliance in the joint design. Controlling joint torque allows shaping the interaction behavior between the human and the robot [14]. However, obtaining a desired link-side dynamics from the motor involves a fourth-order dynamics, as stated in [15]. The complexity is even higher when motor inertia is not negligible; in this case, controlling joint torque allows acting directly on the link-side dynamics.

Despite SEAs providing a direct estimate of the joint torque, their control can be a challenging task, as the relative degree of torque dynamics is two. For this reason, the joint torque tracking controller usually requires a proportional-derivative controller to guarantee stability and accuracy [16]. However,

the derivative term cannot always be used: when the desired torque is a function of both link position and speed, calculating the derivative term requires observing the link acceleration. As a result, the noise due to numerical differentiation is amplified by the derivative gain.

Kim *et al.* [15] demonstrated that introducing physical damping in SEAs is useful to reduce the joint torque dynamics degree to one, and to obtain a stable controller also in case of hard impacts. In literature, several compliant joints are equipped with physical damping: they rely on magnetorheological effect [17], or friction [18], or pneumatic/hydraulic damping [4]. However, the proposed design is not cheap, nor simple, nor enough compact to be embedded in a portable exoskeleton. Furthermore, Kim [19] and Parietti [20] make use of viscoelastic compliant element - i.e. elastomers - but none of them propose a rotative and compact design.

To obtain a solution with the aforementioned features, we investigated the use of silicone elements embedded in the joint, as a simultaneous nonlinear hyper-elastic spring and damper. Austin [21] tried a similar experiment using rubber springs into the joint. The obtained joint presented limits in control performance at high frequency due to the low stiffness of the used rubber and due to hysteresis.

In this paper, the design of a series-viscous-elastic joint with silicone springs is described. Silicone springs exhibits non-linear hyper-elasticity: this feature enhances torque measurement resolution at low torque values and, at the same time, enlarges torque measurement range with equal deformation, compared to linear springs. Moreover, the silicone exhibits an internal damping that allows using a simple proportional control strategy without compromising stability. Concentrating both the elastic and the viscous behaviour into a single element leads to a very compact and thin design, suitable for integration in several applications, as in an exoskeleton joint, or for stable haptic interaction, or collaborative robotics.

## II. MECHANICAL DESIGN

The main requirement for the mechanical design of the SVEJ is suitability for future integration on a portable exoskeleton joint. SVEJ would estimate joint torque and would introduce a compliant element between the actuation and the user without significantly increasing the inertia of the exoskeleton - which affects user motion negatively. The resulting design is a viscous-elastic spring shaped like a disc with a diameter of 10 cm, about ten times larger than the axial thickness of 1 cm. To validate the prototype and to perform characterization, interface parts are designed to allow connection with an ATI torque sensor and a Kollmorgen motor.

### A. Prototype Design

The system is shown in Fig. 2: the input interface (1) is connected to the motor and, on the other side, to the internal gear (2). As shown in Fig. 1, the internal gear and the external gear (3) both have three straight teeth, equally spaced on the circumference and coupled with an angular shift of 60 degrees. The teeth are not directly in contact as there are six equal gaps

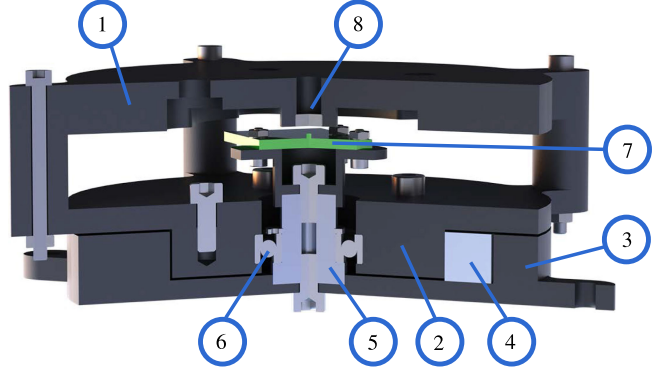


Fig. 2. Section view of the system: 1) Input Interface, 2) Internal Gear, 3) External Gear, 4) silicone Spring, 5) Aluminum shaft, 6) Ball Bearing, 7) Encoder Reading Head, 8) Encoder Magnet.

filled with the silicone springs (4). The silicone springs resist the relative rotation between the two gears, undergoing compression in the circumferential direction. The external gear is connected to the central aluminum shaft (5), which represents the reference axis for the whole mechanism. The ball bearing (6) avoids friction between the shaft and the internal gear. The shaft has a through and fully threaded hole on its axis, where the encoder reading head (7) is fixed using a 3D printed interface. The encoder magnet (8) is fixed on the input interface. Finally, the external gear is the output of the system. The 3D printed parts are made of ABS plastic, while the springs are obtained by pouring commercial liquid silicone rubber in a custom 3D printed mold.

### B. Nonlinear Springs Theoretical Model

The design of the silicone springs is carried out using the Neo-Hookean model for an uncompressible hyperelastic material. When modeling a hyperelastic solid, it is first necessary to define its displacement field, namely the relation between a point in the deformed solid -  $x = (r, \theta, z)$  - and the same point in the undeformed solid -  $X = (R, \Theta, Z)$  -, as shown in Fig. 3. Considering the silicone spring constrained in the radial direction and free in the axial direction, it is possible to write its displacement field in cylindrical coordinates as:

$$r = R \quad \theta = \varepsilon \Theta \quad z = \varepsilon^{-1} Z \quad (1)$$

From the displacement field it is possible to calculate the strain tensor  $A$  as:

$$A = \begin{bmatrix} 1 & 0 & 0 \\ 0 & \varepsilon & 0 \\ 0 & 0 & \varepsilon^{-1} \end{bmatrix} \quad (2)$$

According to the Neo-Hookean model [22] for a hyperelastic material, it is possible to define the strain energy  $W$  stored in the material as:

$$W = C_1 (a_{11}^2 + a_{22}^2 + a_{33}^2 - 3) \quad (3)$$

where  $C_1$  is a constant that depends on the chosen rubber, and the  $a_{ij}$  are the correspondent elements of the  $A$  matrix. The principal stress can be calculated from the strain energy as:

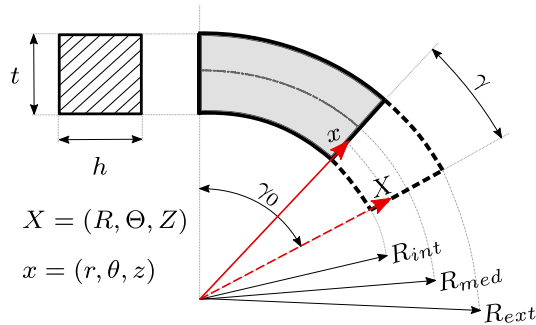


Fig. 3. Silicone spring: definition of the geometrical parameters and the variables of the model.

$$\sigma_i = -p + 2 A_{ii}^2 \frac{dW}{d(A_{ii}^2)} \quad i = 1, 2, 3 \quad (4)$$

where  $p$  is an hydrostatic pressure term that can be calculated imposing that  $\sigma_3 = 0$ , as the silicone spring is hypothesized free in the axial direction. As a result, the circumferential stress can be calculated as:

$$\sigma_2 = 4 C_1 (\varepsilon^2 + \varepsilon^{-2}) \quad (5)$$

Imposing equilibrium of the silicone springs, referring to the parameters defined in Table I, it is possible to write joint torque as:

$$\tau_{load} = 3 F R_{med} = 3 \sigma_2 t h R_{med} = 12 C_1 t h R_{med} (\varepsilon^2 + \varepsilon^{-2}) \quad (6)$$

Finally, it is possible to write  $\varepsilon$ , i.e. the circumferential true strain, as a function of  $\gamma_0$ , i.e. the angular width of the silicone spring, and  $\gamma$ , i.e. the joint angle, measured by the magnetic encoder, as defined in Fig. 3.

$$\tau_{load} = 12 C_1 t h R_{med} \left( \left( \frac{\gamma_0 - |\gamma|}{\gamma_0} \right)^2 + \left( \frac{\gamma_0}{\gamma_0 - |\gamma|} \right)^2 \right) \quad (7)$$

The theoretical relation is determined with only a free constant left that can be calculated experimentally, through characterization tests.

### C. Experimental Characterization

Characterization experiments - setup described in Section IV - are performed to evaluate real system joint torque. In the model described in the previous paragraph, two main factors are not considered, but they are relevant to SVEJ behavior:

- 1) Friction: when gears ‘teeth’ are compressing silicone springs, there is friction between the silicone springs and the external gear, on the springs’ external radius. As a result, hysteresis is expected, with different behaviors between the loading phase and the unloading phase.
- 2) Viscosity: the silicone exhibits internal damping; joint torque is influenced by the deformation rate, too.

In light of that, both static and dynamic characterization experiments are performed. Tests are performed using a motor

TABLE I  
GEOMETRIC PARAMETERS OF THE SILICONE SPRING

$R_{int}$ [mm]	$R_{ext}$ [mm]	$R_{med}$ [mm]	$t$ [mm]	$h$ [mm]	$\gamma_0$ [deg]
30	40	35	10	10	40

with a speed controller. The single test consisted of first loading the joint, increasing the deformation angle at a constant speed until a certain torque value is reached - ranging from 0.5 Nm to 4 Nm -, and then unloading the joint bringing the deformation angle back to 0, at the same constant speed. This loading-unloading cycle is immediately repeated in the other direction of rotation, and then the test is over. Static test speed is about 0.1 deg/s; therefore, viscosity effects are negligible, and only the elastic response of the system is evaluated. The protocol in dynamic experiments is the same, but at higher speed values, ranging from 1 deg/s to 40 deg/s. As shown in Fig. 4, hysteresis, due to friction, is observed in both static and dynamic tests - in this case, due to viscosity, too. The system shows symmetrical and repeatable behavior. From data recorded in static tests, it is possible to build two curves: a loading one and an asymptotic unloading one, reached after a brief transient, as shown in Fig. 4(a). The loading curve is fitted using the theoretical relation (7), obtaining a good matching and an overall estimation error of less than 5%. On the contrary, the asymptotic unloading curve is not well described by the theoretical relation, as stress relaxation, typical of rubber, is not considered in the hyper-elastic material model. However, the unloading curve can be accurately approximated by this power function:

$$\tau_{unload} = c + a |\gamma|^b \quad (8)$$

The data from the dynamic tests, shown in Fig. 4(b), confirms that the amount of torque needed to obtain a certain angular deformation is growing with the increasing speed, in the loading phase, while no significant difference is reported for the unloading curve. The torque difference in loading phase between static tests and dynamic tests is fitted with a function of both deformation rate and deformation angle:

$$\Delta\tau_{dyn} = (m |\gamma| + q) \dot{\gamma} \quad (9)$$

The coefficients found for the three curves are reported in Table II.

### D. Torque Estimator Definition

The estimated torque is defined as a sum of three components:

- 1) Mean static torque  $\tau_{stat}$ , i.e. the mean of static loading and unloading curves.
- 2) Variable static torque  $\Delta\tau_{stat}$ , i.e. the difference between the static loading and unloading curves.
- 3) Dynamic torque  $\Delta\tau_{dyn}$ , as defined in Equation (9).

The mean static torque is defined as:

$$\tau_{stat} = \frac{\tau_{load} + \tau_{unload}}{2} \quad (10)$$

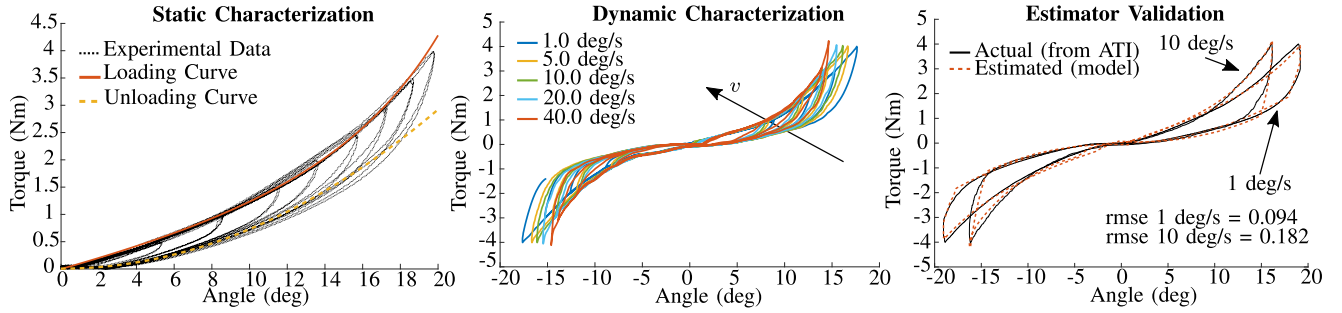


Fig. 4. SVEJ characterization. Left: static characterization experimental data and best fitting loading and unloading curves. Center: experimental data from dynamic characterization for different speeds. Right: Torque estimator validation through simulation.

TABLE II  
COEFFICIENTS RESULTING FROM THE DATA FITTING

$C_1$	$a$	$b$	$c$	$m$	$q$
[kPa]	[Nmm]	[-]	[Nmm]	$\left[ \frac{\text{Nmm}\cdot\text{s}}{\text{deg}^2} \right]$	$\left[ \frac{\text{Nmm}\cdot\text{s}}{\text{deg}} \right]$
21.2	7.1	2.0	6.4	18.7	-32.6

with  $\tau_{load}$  defined as in Equation (7), with the parameters and coefficients as in Table I and in Table II. The variable static torque can be written as:

$$\Delta\tau_{stat} = \frac{\tau_{load} - \tau_{unload}}{2} \quad (11)$$

This contribution is weighed with the coefficient  $\alpha_{stat}$ , depending on the history of the system, ranging from  $-1$  to  $1$ . This coefficient is calculated as:

$$\alpha_{stat} = \frac{\sum_{i=k-N+1}^k \text{sign}(\gamma) \text{sign}(\dot{\gamma})}{N} \quad (12)$$

The coefficient increases when the angle and the speed are concordant, so when the SVEJ is under load. On the contrary, when the signs are discordant, the SVEJ undergoes an unloading phase and the coefficient decreases. Using the mean value over the last  $N$  samples recorded allows smoother transitions for the estimated torque from the loading curve to the unloading curve, and vice-versa. This feature allows enhancing joint torque estimate and helps controller stability. The number  $N$  of samples chosen is 500; it is validated through simulation of the estimated torque using angle and torque data from the tests, as shown in Fig. 4(c). The computed RMS errors are below 0.2 Nm, i.e. 5% of the maximum torque  $-4$  Nm - which is an acceptable result. Timestep of the real-time controller is taken into account, too - a stability condition for the transition function can be found in [23]. The sign function is used to attribute a direction to the estimated torque. Finally, the torque estimator of the system is:

$$\hat{\tau}_j = \text{sign}(\gamma) (\tau_{stat} + \alpha_{stat} \Delta\tau_{stat} + \Delta\tau_{dyn}) \quad (13)$$

### III. CONTROL STRATEGY

Fig. 5 shows the schema of a linearized model of the joint that is useful to derive a simple control law and to recall a concept expressed in [15], i.e. the physical damping can simplify

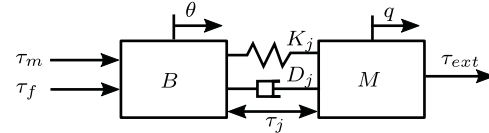


Fig. 5. Schema of the visco-elastic joint, as in [15].

the controller structure. The dynamic equations of the joint can be written as:

$$B\ddot{\theta} + \tau_j = \tau_m \quad (14)$$

$$M\ddot{q} = \tau_j + \tau_{ext} \quad (15)$$

where  $\tau_j$  is the joint torque, that is observable as it can be approximately calculated as in (13).  $B$  is the motor-side inertia,  $M$  is the link-side inertia,  $\theta$  is the motor angle, and  $q$  is the link angle.  $\tau_m$  is the motor torque, and  $\tau_{ext}$  is the external torque applied to the link - the interaction torque, hence the controlled output.

The deformation angle  $\gamma$  of the SVEJ, measured by the magnetic encoder and defined as in Equation (7) and Fig. 3, can be written as:

$$\gamma = \theta - q \quad (16)$$

The linearized model of the joint torque is given by:

$$\tau_j = K_j(\theta - q) + D_j(\dot{\theta} - \dot{q}) \quad (17)$$

Differentiating two times Eqn (17) and using Eqn (14), we obtain:

$$\ddot{\tau}_j = K_j(B^{-1}(-\tau_j + \tau_m) - \ddot{q}) + D_j(B^{-1}(-\dot{\tau}_j + \dot{\tau}_m) - \ddot{q}) \quad (18)$$

Given this torque dynamics, it is possible to use the  $\tau_m$ :

$$\tau_m = B\ddot{q} + \tau_j + u \quad (19)$$

where  $u$  represents the control law, and the other two terms can be considered as compensation contributions to the controller. With this  $\tau_m$ , the joint torque dynamics becomes:

$$\ddot{\tau}_j = K_j u + D_j \dot{u} \quad (20)$$

where it is possible to notice that the physical damping already introduces a derivative (D) contribution, even if the chosen

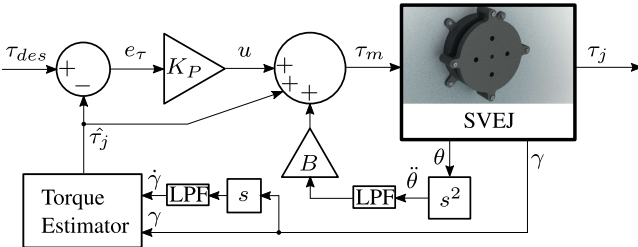


Fig. 6. Torque controller architecture. LPF stands for low pass filter.

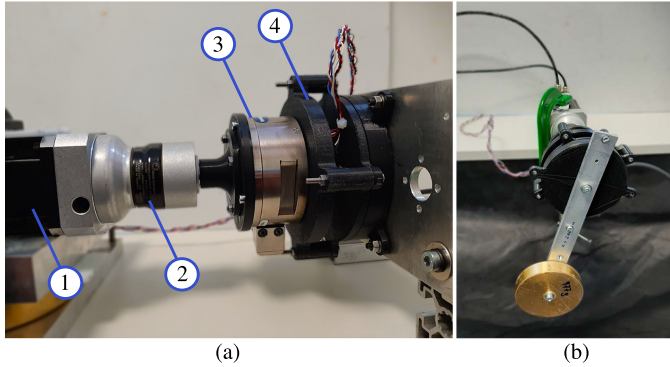


Fig. 7. a) Experimental setup with the fixed output link, used for mechanical characterization and bandwidth evaluation: 1) Kollmorgen Motor AKM2F, 2) Apex gear drive (1:10), 3) 6-axes ATI Torque sensor, 4) SVEJ; b) Experimental setup with the free output link composed of an aluminum lever and a brass weight, used for transparency - without the brass weight - and impact tests.

control law for  $u$  is just a proportional (P) one. As a result, we choose the control law:

$$u = -BK_P(\tau_{des} - \tau_j) = -BK_Pe_\tau \quad (21)$$

The schema of the implemented controller is depicted in Fig. 6. Finally, it is possible to show that the error dynamics in closed-loop - Eqn (22) - is stable around the equilibrium point  $\tau_j = \tau_{des}$  because all the coefficients of the equation are positive, and, therefore, the Routh-Hurwitz criterion is satisfied.:

$$\ddot{\tau}_j + K_P D_j \dot{e}_\tau + K_P K_j e_\tau = 0 \quad (22)$$

With this control strategy, it is possible to simulate a compliance behavior, around a fixed position  $q_{des}$ , by generating a reference  $\tau_{des}$  signal:

$$\tau_{des} = K_d(q_{des} - q) - D_d \dot{q} \quad (23)$$

The main advantage given by the combination of the physical damping and a P-control law instead of a PD-controller is the possibility to exclude the calculation of  $\dot{e}_\tau$ , requiring  $\ddot{q}$ , which is generally a signal affected by noise, hence contributing to instability. Despite using  $\ddot{q}$  for the compensation term  $B\ddot{q}$ , no control gain amplifies the acceleration noise, as it would happen if using a PD-controller. However, the fixed physical damping value constrains the choice of the proportional gain because of the limited phase margin.

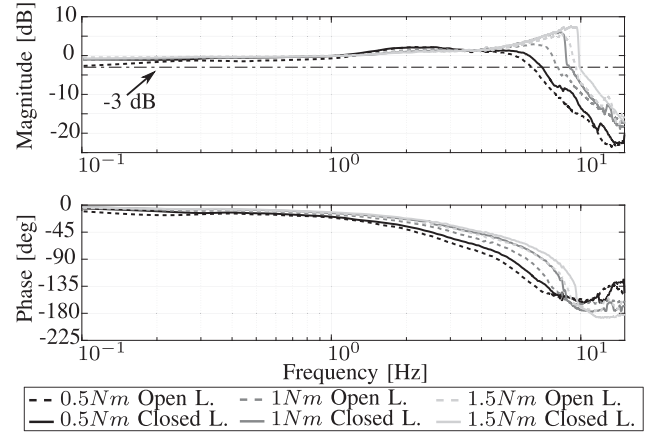


Fig. 8. Bode Diagram of the SVEJ: the system exhibits a behavior that can be approximated by a linear second-order dynamics with input amplitude dependent parameters. With a  $0.5 \text{ Nm}$  chirp input torque, the bandwidth is  $6.3 \text{ Hz}$  in the open-loop (OL) condition and  $6.9 \text{ Hz}$  in the closed-loop (CL) condition. These values become  $8.1 \text{ Hz}$  (OL) and  $9.1 \text{ Hz}$  (CL) for  $1 \text{ Nm}$  amplitude, and  $9.6 \text{ Hz}$  (OL) and  $9.9 \text{ Hz}$  (CL) for  $1.5 \text{ Nm}$  amplitude. Torque measurements come from ATI torque sensor.

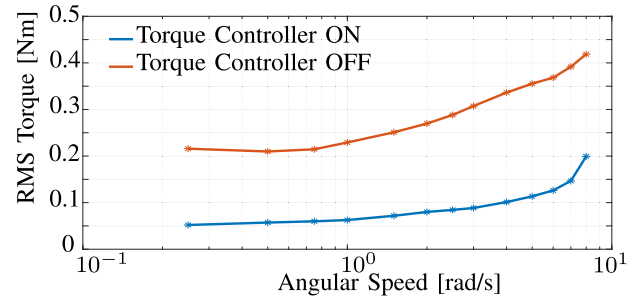


Fig. 9. Transparency Test: RMS torque calculated for different angular speed values. Torque measurements come from ATI torque sensor.

## IV. EXPERIMENTS AND RESULTS

### A. Experimental Setup

The experimental setup - Fig. 7 - consists of a Kollmorgen motor (AKM23F, continuous torque  $1.1 \text{ Nm}$ ), connected to an Apex Dynamics PG II 040 gear drive (1:10, efficiency  $> 97\%$ ) driving the SVEJ. The motor has got an integrated encoder with a resolution of 13 bits. Between the motor and the SVEJ, an ATI gamma F/T sensor - 6 axes - is installed, with a torque range of  $\pm 10 \text{ Nm}$ . The F/T sensor is only for characterization and controller evaluation purposes, and it is not used to drive the joint. The relative rotation between motor output and the link is measured by an AMS-AS5047P magnetic encoder with a resolution of 12 bits. The torque controller is implemented through MATLAB Simulink Real-Time on a mini-pc, running at  $2 \text{ kHz}$ . The overall motor-side inertia, taking into account motor, gear drive, and internal gear of the SVEJ, is about  $0.06 \text{ Kg}\cdot\text{cm}^2$ . The link is made of an aluminum lever and a brass weight of  $0.978 \text{ Kg}$ .

### B. Bandwidth

The experimental setup used for the evaluation of the bandwidth is shown in Fig. 7a. During this test, the output link is

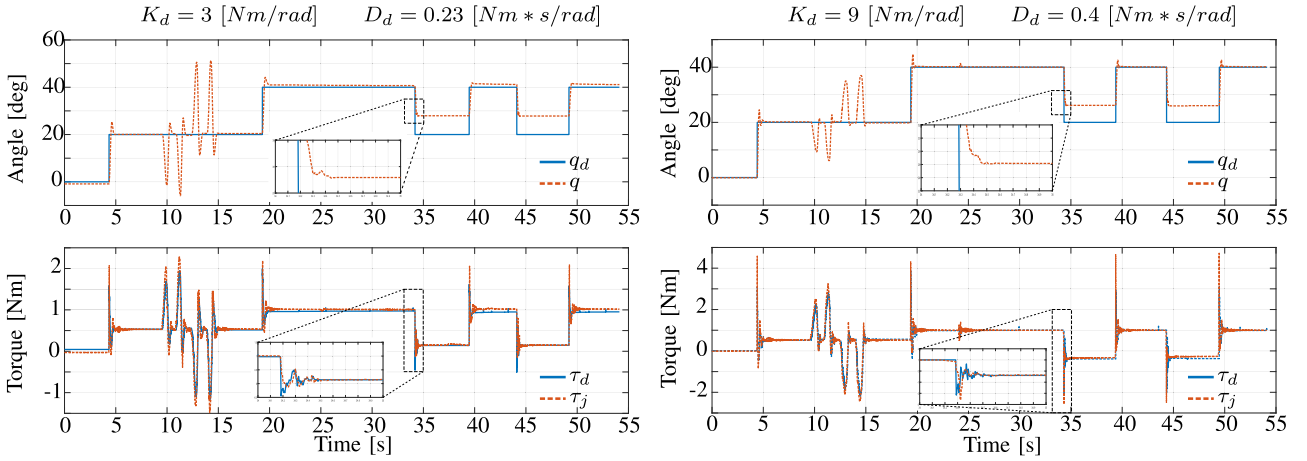


Fig. 10. Impact test with a) low impedance, b) high impedance. Desired (blue) and measured (orange) angle and torque during the test. At 5 s, the desired angle is switched from 0 to 20 degs. From 10 s to 15 s, the system is manually moved. At 20 s, the desired angle is switched from 20 degs to 40 degs. At about 35 s, the first impact happens, and the link remains in contact with the obstacle for five seconds. At 40 s, the desired angle is switched back to 40 degs. At 45 s, the second impact happens, and the link remains in contact with the obstacle for five seconds. At 50 s, the system is brought back at 40 degs, and at 55 s the test is over. Torque measurements come from ATI torque sensor.

locked, i.e. the link mass can be considered equal to infinite, and the motor angle  $\theta$  is always equal to the deformation angle  $\gamma$ . Open-loop and closed-loop responses are evaluated by exciting the system with a chirp input torque ranging from 0.1 to 15 Hz, at three different amplitudes  $-0.5$ ,  $1$  and  $1.5$  Nm, as shown in Fig. 8 to exploit system nonlinearity. In this setup condition, the linearized system exhibits two complex and conjugated poles. When exciting the system with a chirp input torque, the increasing amplitude corresponds to a shifting of the poles of the linearized system towards marginal stability. Consequently, the phase margin lessens with increasing amplitude. For these reasons, only a small proportional gain can be used with a purely proportional control law, and a slight increment of the bandwidth can be achieved.

### C. Transparency

In the transparency test, the output link is manually moved by an operator, which tries to track a desired minimum jerk trajectory plotted on-screen in real-time. The experimental setup for the test is as shown in Fig. 7(b), except that the brass weight is not mounted on the link to avoid excessive inertial effects on the evaluation of joint transparency. The experiment is performed in two different conditions - Controller OFF and Controller ON -, and it is repeated for different link speed values, ranging from  $0.25$  rad/s to  $8$  rad/s. The results - Fig. 9 - show a significant reduction of the RMS torque between the controller OFF condition - ranging from  $0.22$  Nm to  $0.42$  Nm - to the controller ON condition - ranging from  $0.05$  Nm to  $0.2$  Nm.

### D. Impedance Rendering and Impact

In the impedance rendering/impact test, the desired torque signal is function of the parameters of a required virtual impedance. Two different values of impedance are selected as reported in Fig. 10, called respectively “low impedance” and “high impedance”. The experimental setup is as shown in Fig. 7(b); for equilibrium reasons, gravity compensation, dependent from

the desired rest angle  $q_d$  of the simulated impedance, is included in the desired torque to balance the brass weight. Given this, the desired torque is:

$$\tau_d = -K_d(q - q_d) - D_d\dot{q} + mgl \cdot \sin(q_d) \quad (24)$$

During the test the desired angle is changed according to the protocol described in Fig. 10, which shows the data collected during the experiment. The controller guarantees a stable response to the variation of the desired angle, both with high and low impedance. When manually disturbing the system at 20 degs, the controller can track the desired torque with good precision and stability. Nevertheless, the system exhibits a torque overshoot when the reference angle is suddenly changed from one value to another as the effect of the system’s second-order torque dynamics in conjunction with the use of a linear proportional controller. During the impacts, the angle signal keeps smooth, and the torque transient lasts about  $0.3$  s, thus meaning that the transient oscillations are fastly damped by the intrinsic damping of the system.

## V. CONCLUSION

In this paper, a novel design for a series-elastic joint with physical damping is proposed. Joint torque has been characterized, hence it is possible to estimate the torque by measuring the deformation angle and the deformation rate of the joint. A simple proportional controller has been used to investigate joint performance in bandwidth, transparency, impedance rendering, and stability. The device is lightweight  $-0.175$  kg - and cheap, and it is suitable for future integration in an exoskeleton joint as a torque sensor [24]. The main novelty of this design is the integration of both elastic and viscous behaviors in a single element, i.e. the silicone spring, that allows a compact design.

The characterization experiments have shown a repeatable behavior for the system, even if slightly different torque values have been reported between different records of the same loading-unloading cycle. Moreover, the curves that have been built

through data fitting, as shown in Fig. 4, introduce another source of inaccuracy, compared to experimental data. However, the overall low error in torque estimate does not compromise using the SVEJ as a torque sensor to perform torque control, as shown in the experiments regarding bandwidth, transparency and impedance rendering. The impacts during the impedance rendering experiment have not caused instability, confirming the reliability of the proportional controller. The controlled system bandwidth –6.9 Hz, 9.1 Hz, and 9.9 Hz respectively at 0.5 Nm, 1.0 Nm, and 1.5 Nm chirp amplitude- and the joint natural impedance - evaluated in the transparency test - are in agreement with literature results (e.g. as in [21]). Moreover, the transparency has been evaluated for a range of speed comparable to the typical frequencies of human arm motion, proving system suitability for different tasks feasible with an exoskeleton. Compared with existing literature designs [18], [21], our solution allows a compact design while showing similar performances and preserving system stability with a simple proportional controller. The estimate still needs to be refined to allow improving torque measurement accuracy, and a nonlinear controller could be used to enhance control performance. Besides, the 3D printed components and the silicone springs of this prototype do not allow exerting torque values of about 10 Nm, as it is required in shoulder exoskeleton. However, silicone springs, or more in general rubber springs, seem to be promising to enhance the performance of series-elastic elements used in the human-robot interaction field, for applications such as cooperative robotics and exoskeletons.

## REFERENCES

- [1] N. Vitiello *et al.*, “NEUROExos: A powered elbow exoskeleton for physical rehabilitation,” *IEEE Trans. Robot.*, vol. 29, no. 1, pp. 220–235, Feb. 2013.
- [2] K. Kong, J. Bae, and M. Tomizuka, “A compact rotary series elastic actuator for human assistive systems,” *IEEE/ASME Trans. Mechatronics*, vol. 17, no. 2, pp. 288–297, Apr. 2012.
- [3] M. Zinn, O. Khatib, B. Roth, and J. K. Salisbury, “Playing it safe [human-friendly robots],” *IEEE Robot. Autom. Mag.*, vol. 11, no. 2, pp. 12–21, Jun. 2004.
- [4] J. Oblak and Z. Matjačić, “Design of a series visco-elastic actuator for multi-purpose rehabilitation haptic device,” *J. Neuroengineering Rehabil.*, to be published, doi: 10.1186/1743-0003-8-3.
- [5] R. Schiavi, G. Grioli, S. Sen, and A. Bicchi, “VSA-II: A novel prototype of variable stiffness actuator for safe and performing robots interacting with humans,” in *Proc. IEEE Int. Conf. Robot. Autom.*, 2008, pp. 2171–2176.
- [6] B. Vanderborght, N. G. Tsagarakis, C. Semini, R. Van Ham, and D. G. Caldwell, “MACCEPA 2.0: Adjustable compliant actuator with stiffening characteristic for energy efficient hopping,” in *Proc. IEEE Int. Conf. Robot. Autom.*, 2009, pp. 544–549.
- [7] G. A. Pratt and M. M. Williamson, “Series elastic actuators,” in *Proc. IEEE/RSJ Int. Conf. Intell. Robots Syst. Human Robot Interact. Cooperative Robots*, 1995, vol. 1, pp. 399–406.
- [8] S. Wolf *et al.*, “Variable stiffness actuators: Review on design and components,” *IEEE/ASME Trans. Mechatronics*, vol. 21, no. 5, pp. 2418–2430, Oct. 2016.
- [9] B. Vanderborght *et al.*, “Variable impedance actuators: A review,” *Robot. Auton. Syst.*, vol. 61, no. 12, pp. 1601–1614, 2013.
- [10] N. Kashiri, J. Malzahn, and N. G. Tsagarakis, “On the sensor design of torque controlled actuators: A comparison study of strain gauge and encoder-based principles,” *IEEE Robot. Autom. Lett.*, vol. 2, no. 2, pp. 1186–1194, Apr. 2017.
- [11] W. Roozing, J. Malzahn, N. Kashiri, D. G. Caldwell, and N. G. Tsagarakis, “On the stiffness selection for torque-controlled series-elastic actuators,” *IEEE Robot. Autom. Lett.*, vol. 2, no. 4, pp. 2255–2262, Oct. 2017.
- [12] I. Thorson and D. Caldwell, “A nonlinear series elastic actuator for highly dynamic motions,” in *Proc. IEEE/RSJ Int. Conf. Intell. Robots Syst.*, 2011, pp. 390–394.
- [13] J. Malzahn, E. Barrett, and N. Tsagarakis, “A rolling flexure mechanism for progressive stiffness actuators,” in *Proc. Int. Conf. Robot. Autom.*, 2019, pp. 8415–8421.
- [14] K. Kong, J. Bae, and M. Tomizuka, “Control of rotary series elastic actuator for ideal force-mode actuation in human–robot interaction applications,” *IEEE/ASME Trans. Mechatronics*, vol. 14, no. 1, pp. 105–118, Feb. 2009.
- [15] M. J. Kim, A. Werner, F. C. Loeffl, and C. Ott, “Enhancing joint torque control of series elastic actuators with physical damping,” in *Proc. IEEE Int. Conf. Robot. Autom.*, 2017, pp. 1227–1234.
- [16] S. Yoo and W. K. Chung, “Sea force/torque servo control with model-based robust motion control and link-side motion feedback,” in *Proc. IEEE Int. Conf. Robot. Autom.*, 2015, pp. 1042–1048.
- [17] C.-M. Chew, G.-S. Hong, and W. Zhou, “Series damper actuator: a novel force/torque control actuator,” in *Proc. 4th IEEE/RAS Int. Conf. Humanoid Robots*, 2004, pp. 533–546.
- [18] D. Accoto, N. L. Tagliamonte, G. Carpino, F. Sergi, M. Di Palo, and E. Guglielmi, “PVEJ: A modular passive viscoelastic joint for assistive wearable robots,” in *Proc. IEEE Int. Conf. Robot. Autom.*, 2012, pp. 3361–3366.
- [19] D. Kim, J. Ahn, O. Campbell, N. Paine, and L. Sentis, “Investigations of a robotic test bed with viscoelastic liquid cooled actuators,” *IEEE/ASME Trans. Mechatronics*, vol. 23, no. 6, pp. 2704–2714, Dec. 2018.
- [20] F. Parietti, G. Baud-Bovy, E. Gatti, R. Riener, L. Guzzella, and H. Vallery, “Series viscoelastic actuators can match human force perception,” *IEEE/ASME Trans. Mechatronics*, vol. 16, no. 5, pp. 853–860, Oct. 2011.
- [21] J. Austin, A. Schepelmann, and H. Geyer, “Control and evaluation of series elastic actuators with nonlinear rubber springs,” in *Proc. IEEE/RSJ Int. Conf. Intell. Robots Systems*, 2015, pp. 6563–6568.
- [22] R. W. Ogden, *Non-Linear Elastic Deformations*. Chelmsford, MA, USA: Courier Corporation, 1997.
- [23] D. Chiaradia, M. Solazzi, D. Caporali, M. Russo, A. Piu, and A. Frisoli, “Haptic simulation of an automotive automatic gearshift: Stability analysis and design of force profiles with hysteresis,” in *Proc. IEEE Int. Conf. Robot. Autom.*, pp. 2663–2668, 2016.
- [24] L. Tiseni, M. Xiloyannis, D. Chiaradia, N. Lotti, M. Solazzi, H. van der Kooij, A. Frisoli, and L. Masia, “On the edge between soft and rigid: an assistive shoulder exoskeleton with hyper-redundant kinematics,” in *Proc. IEEE 16th Int. Conf. Rehabil. Robot.*, 2019, pp. 618–624.